Design of a Lightweight Dual Arm System for Aerial Manipulation

Alejandro Suarez, Antonio Enrique Jimenez-Cano, Victor Manuel Vega, Guillermo Heredia, Angel Rodriguez-Castaño, and Anibal Ollero

Robotics, Vision and Control Group – University of Seville, Camino de los Descubrimientos, s/n, 41092, Seville (Spain)

E-mail addresses: asuarezfm@us.es (A. Suarez), antenr@hotmail.com (A. E. Jimenez-Cano), victorvegaes@gmail.com (V. M. Vega), guiller@us.es (G. Heredia), castano@us.es (A. Rodriguez-Castaño), aollero@us.es (A. Ollero)

ABSTRACT

This paper presents the development and experimental validation of a low weight and inertia, human-size and highly dexterous dual arm system designed for aerial manipulation with multirotor platform. The arms, weighting 1.8 kg in total and with a maximum lift load per arm around 0.75 kg, provide five degrees of freedom (DOF) for end-effector positioning and wrist orientation. A customized aluminium frame structure supports the servo actuators, placing most part of the mass close to the shoulder structure in order to reduce the inertia. A double flange bearing mechanism in side-by-side configuration isolates the servos from impacts and radial/axial overloads, increasing robustness. This is important to prevent that the arms are damaged during physical interactions with the environment, as they should support the kinetic energy of the whole platform. The motivation in the development of a dual arm aerial manipulator is extending the range of applications and tasks that can be performed with respect to the single arm case, like grasping large objects or assembling. The paper covers the kinematic and dynamic modelling of the aerial robot, proposing a control scheme that deals with the technological limitations of the smart servo actuators. The performance of the arms and the interactions with the aerial platform are evaluated in test bench experiments. The proposed dual arm design is validated through outdoor flight tests with two commercial hexarotor platforms equipped with standard industrial autopilots.

***Keywords**: dual arm aerial manipulation, lightweight dual arm*

1. Introduction

1.1. State of the art in aerial manipulation

The aerial manipulation field extends the range of applications of vertical take-off and landing (VTOL) unmanned aerial vehicles (UAVs), either autonomous helicopters or multi-rotors [1][2][3]. Including one or more robotic arms in an aerial platform allows the execution of different inspection and maintenance tasks in industrial scenarios of difficult access for human operators in both indoors [4] and outdoors [5], reducing the time and cost associated to the deployment of persons, vehicles, cranes and tools typically employed. Some examples include inspection and maintenance of high altitude pipes in chemical plants [6], structure constructions [7], installation and retrieval of sensor devices in polluted areas, repair of cracks in the blades of wind turbines, or replacing the batteries of remote robots. The effort now is focused in the development of low weight grippers and robotic arms to be integrated in these vehicles. Several mechanisms have been proposed. Quadrotor grasping and perching using impactive and ingressive grippers is presented in [7]. A simple 2-DOF robotic arm, 0.37 kg weight and 0.32 m length, is shown in [9]. Valve turning on flight with a quadrotor is demonstrated in [10] with two 2-DOF arms, generating a torque in the yaw angle with the propellers while grasping the valve. A large hexarotor platform equipped with two teleoperated arms has been presented for object transportation [11]. The 5 DOF lightweight robotic arm presented in [11] reduces the inertia of the manipulator employing timing belts for transmitting the motion from the actuators placed at the base to the joints. The single DOF arm with flexible joint developed in [13] employs a Dynamixel servo as actuator and a pair of extension springs as transmission mechanism between the servo pulley and the link pulley.

In our previous work, we developed two prototypes of lightweight and compliant arms for aerial manipulation. Reference [14] is a particular implementation of the Series Elastic Actuators [15], consisting of a linear actuator and a pair of extension springs acting as elastic tendons on the elbow joint, used for estimating the payload at the wrist point but also for detecting collisions on the forearm. Mechanical joint compliance with deflection measurement allows the estimation and control of the contact forces in a 3-DOF arm [16]. **Table 1** compares the proposed design w.r.t. other prototypes intended to aerial manipulation. Note that this manipulator provides the highest number of DOF's and maximum lift load and reach.

Table 1. Comparison of different prototypes of lightweight robotic arms for aerial manipulation.

Reference	Single / Dual Arm	Stiff / Compliant	Total DOF's	Weight/Max. lift load* [kg]	Reach [m]	Max. stall torque [N·m]	Actuators
Proposed	Dual	Stiff	10	1.8 / 0.75*	0.5	7.5	Herkulex
[10]	Dual	Stiff	4	NA / NA	NA	3.1	Dynamixel
[11]	Dual	Stiff	NA	NA / NA	NA	NA	NA
[9]	Single	Stiff	2	0.37 / NA	0.32	3.1	Dynamixel
[43]	Single	Stiff	6	1.4 / NA	0.45	10.0	Dynamixel
[11]	Single	Stiff	5	0.25 / 0.2	0.3	1.2	DC motor
[13]	Single	Compliant	1	0.36 / NA	0.18	1.5	Dynamixel
[16]	Single	Compliant	3	0.3 / 0.2*	0.5	1.17	Herkulex
[17]	Dual	Compliant	8	1.3 / 0.2*	0.5	2.34	Herkulex

*. Maximum lift load per arm in the worst case (0 – 90 degrees rotation in the shoulder pitch joint)

Bimanual manipulation with multi-rotors has been addressed only in a few recent works [10][11][17]. However, dual arm manipulators have been already considered in space applications for several years [26]. In this sense, the redundancy provided by a second arm in a free-floating space robot can be exploited for optimizing the torque control of the whole manipulator [27], planning the trajectories of the arms in such a way that robot base is stabilized [28]. Several control methods have been developed and tested in dual arm systems with fixed or mobile base. Reference [29] deals with the cooperative control of two 3-DOF flexible link manipulators when holding an object in a closed kinematic chain. Dexterous manipulation with DLR humanoid robot Justin is shown in [30]. Impedance control is evaluated in [31] with two 6-DOF industrial manipulators. Cartesian impedance control is also applied for the real-time motion tracking in an anthropomorphic dual arm [32]. An extensive survey on other dual arm systems can be found in [33].

One of the main problems in the control of an aerial manipulation robot is the influence of arms motion over UAV attitude due to the dynamic coupling between both parts. Different control schemes have been proposed and experimentally validated with multi-rotor platforms, including PI-D [18], variable parameter integral backstepping [2], adaptive controllers [19], and other multi-layer architectures [20][21]. When the aerial platform is intended to perform grasping and transportation operations, it results convenient to have a method for estimating the weight of the grasped object, and hence its influence on the UAV dynamic behavior [22][23]. Helicopter stability is analyzed in [24] when contact forces are introduced in the aircraft through a compliant end-effector attached to the base employed for object grasping. The stability of a PID controller for flight control during object grasping and release operations is demonstrated in simulation and experimentally. Ref. [25] presents a control architecture for compliant interaction between a quadrotor equipped with an n-DOF manipulator and the environment.

1.2. Contribution of this work

This paper describes a dual arm aerial manipulator for outdoor operation consisting of a human size dual arm integrated in a commercial hexarotor. Whereas most aerial manipulators that can be found in the literature are research prototypes evaluated in indoor testbeds, the proposed dual arm design extends the range of tasks that can be accomplished with respect to the single arm case, satisfying four requirements essential in the successful application of the aerial manipulation technology outdoors: 1) high payload (up to 0.75 kg per arm) for manipulating a wide variety of objects and tools, 2) high joint/Cartesian speed (300

deg/s, 2.5 m/s at end effector) for agile task execution, 3) positioning accuracy and reliability for object grasping, and 4) mechanical robustness for extending the lifespan of the actuators. The manipulator is built with smart servo actuators and a customized anodized aluminium frame structure that reduces the manufacturing cost. The accuracy, repeatability and smoothness in the operation of the arms is evaluated in test bench experiments. The paper also addresses their integration in a hexarotor platform, including the identification of motion constraints and the electronics. The kinematics and dynamics of the dual arm aerial manipulator are derived, proposing a control scheme that makes use of the manipulator dynamics for compensating the reaction wrenches. The interactions between the manipulator and the aerial platform are experimentally identified in testbench in hovering conditions. Finally, the dual arm design is validated through an extensive set of outdoor flight tests with two commercial hexarotor platforms equipped with standard industrial autopilots (**Fig. 1**), showing that the influence of high speed motions of the arms over the aerial vehicle is low. The video of the flight tests is provided as attachment, or it can be seen in [44].

Fig. 1. Developed lightweight and human-size dual arm manipulator integrated in two hexarotor platforms. Outdoor flight tests.

The rest of the paper is organized as follows. Section II begins detailing the motivations for considering a dual arm robot in aerial manipulation applications. The design requirements are then presented and followed by the description of the developed dual arm. Section III describes the aerial manipulator, including its specifications, the electronics, and the motion constraints for the arms. Section IV describes the kinematics and dynamics of the dual arm system, proposing a control scheme for the aerial manipulator in Section V. Experimental results are presented in Section VI, summarizing the conclusions in Section VI.

2. Dual arm system description

2.1. Motivation

A dual arm system extends the grasping and manipulation capabilities that can be performed with an aerial platform with respect to the single arm case, allowing the simultaneous grasping and transportation of two objects, or large objects than cannot be handled with a single arm (**Fig. 2** left). It makes possible the execution of certain tasks that are more suitable for a dual arm manipulator, like assembly or insertion operations. Manual operations assisted with visual feedback can be also performed with a camera in eye-in-hand configuration (**Fig. 2** right). This is done at expenses of increasing the mass of the manipulator, although the payload to weight ratio is not significantly increased with respect to the single arm case.

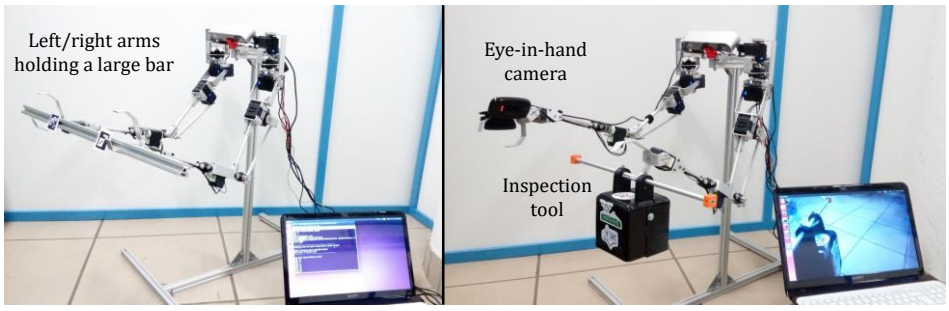

Fig. 2. Two illustrative application examples of the lightweight and human-size dual arm manipulator with ZED camera head.

2.2. Design considerations

2.2.1. Low weight and inertia features

The main design criteria imposed to the arms was reducing the weight and inertia as much as possible, so the payload of the multirotor is not exceeded and the influence of arms motion over UAV stability is not significant. Let us call PL_{UAV} to the available payload of the multirotor, and m_{DAM} and PL_{DAM} to the weight and maximum payload of the dual arm manipulator. The following design equation is then derived:

$$m_{DAM} + PL_{DAM} \leq \eta \cdot PL_{UAV} \quad , \quad \eta \in [0, 1) \tag{1}$$

Here $\eta \cong 0.7$ is a design constant that indicates the operation regime of the brushless motors. In case the aerial platform is overloaded ($\eta > 0.8$), the motors will not respond properly to the control signals, as they will be operating close to the saturation zone. Low inertia is achieved placing the servos close to the shoulder structure, using rigid bars for transmitting the motion from the actuator to the joint in some cases.

2.2.2. Actuators

Smart servos like Herkulex or Dynamixel are currently the best option for building low weight robotic arms due to their features: low cost, high torque to weight ratio, compact design, easy integration and assembly, embedded electronics, high accuracy and precision control. From our experience, the stall torque parameter given by the manufacturer should be taken with care, in the sense that in practice it should be around two times higher than the required dynamic torque. Otherwise, the arms will not be able to lift the expected load. These actuators also present some technological limitations in terms of control and feedback capability that have to be taken into account when designing the control system. First of all, servo acceleration/torque control or feedback is not available. Only the position, and in some models the speed, can be commanded. The update rate in these devices is typically under 100 Hz, limited by the embedded controller and the serial communication bus. The alternative to this solution is the development of customized actuators using Maxon or Faulhaber motors. However, the main problem now is the design and construction of the gearbox, which should be compact, very low weight (below 0.1 kg), with reduction ratios around 150:1 and mechanically robust.

2.2.3. Materials for the frame structure

The most suitable materials for building the frame parts of the arms are aluminum and carbon fiber due to their low mass density, low cost and high mechanical resistance. Aluminum is however preferred for the development of prototypes as most frames can be manufactured using hand tools, it can be bended for building L-shape or U-shape frames, and because its manufacturing process is less toxic to human health. Plastic frames were rejected due to their low mechanical and thermal resistance, preventing the waste of time replacing damaged parts due to impacts or high temperatures during the realization of experiments in outdoors. The mechanical protection of the servos is an important issue, as it extends their lifespan, reduces the time and cost of repairs and increases the reliability. It is highly desirable that radial and axial loads exerted over the arms are supported by the frame structure instead of directly exposing the actuators to them. Polymer flange bearings (igus EFOM/EFSM) attached at the aluminum frame structure are suitable components for this purpose due to their low mass density (1.49 g/cm^3 vs 8.75 g/cm^3 of steel) and because they provide vibration damping.

2.3. Dual arm design

2.3.1. General overview

A rendered view of the 3D model of the arms is depicted in **Fig. 3**. From top (shoulder) to bottom (wrist) the joints are: shoulder yaw, shoulder pitch, elbow pitch, wrist roll and wrist pitch. The kinematic configuration of the shoulder was chosen in such a way that the equations of the kinematic and dynamic models result in the simplest form, which reduces the computational cost and simplifies the control, and at the same time the working space is maximized. The actuators employed are the Herkulex smart servos from Dongbu Robot. These servos integrate the motor, gears, electronics and communications in a compact and robust device, providing very high torque to weight ratio and extensive information about the internal state

of the servo, such like position, speed, PWM, temperature or voltage. The model of the servos and the main parameters associated to each joint are listed in **Table 2**. The different frames of the arms have been designed in such a way that they can be easily manufactured using hand tools from standard anodized aluminum profiles, including 15×2, 20×2 and 30×2 mm flat profiles, and 8 mm Ø hollow circular profile.

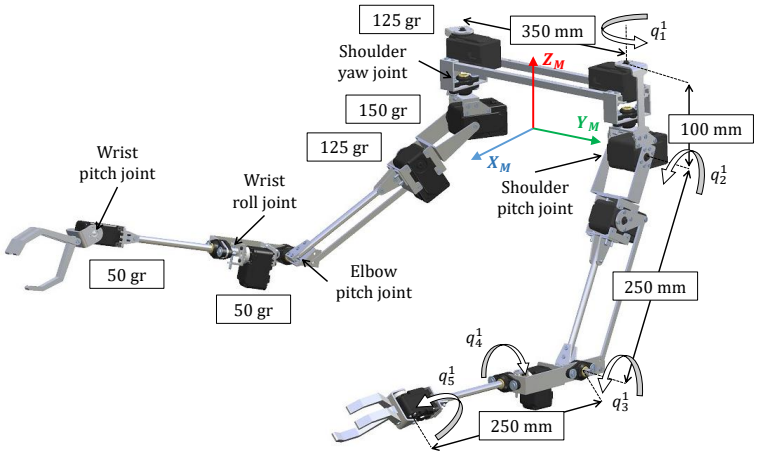

Fig. 3. Rendered view of the 10-DOF lightweight dual arm manipulator with the significant lengths and joint angles.

Table 2. Specifications of the arm joints.

Joint	Servo Model	Stall torque [N·m]	Rotation range [deg]	Actuator weight [gr]
Shoulder Yaw	Herkulex DRS-0402	5,1	±90	125
Shoulder Pitch	Herkulex DRS-0602	7,6	±90	150
Elbow Pitch	Herkulex DRS-0402	5,1	[30, 150]	125
Wrist Roll	Herkulex DRS-0101	1,17	±150	50
Wrist Pitch	Herkulex DRS-0101	1,17	±135	50

2.3.2. Mechanical servo protection

As mentioned before, one of the key aspects in the design of the arms is protecting the servos against unexpected and undesired impacts and loads so they are not damaged. Some typical situations include crashes of the aerial platform against the floor, impacts of the arms against the landing gear, or, in the case of a dual arm, closed kinematic chains. Note that the cost of the servos represents approximately the 80% of the cost in materials. In the proposed design, six pairs of igus® EFOM-08 flange bearings in side-by-side configuration are employed for reducing the radial and axial load exerted over elbow pitch and wrist yaw servos (**Fig. 4**), and over shoulder yaw servo (**Fig. 5**). This simple and low weight mechanism (20 grams), distributes the load through the aluminium frames, isolating the servos from overloads. The space left between the servo shaft and the output link can be exploited for providing compliance introducing a flexible coupling element like springs [15], although this is out of the scope of this work. This mechanism was not considered in the shoulder and wrist pitch joints due to space limitations.

2.3.3. Design of the frame structure

The dual arm manipulator consists of fifty two aluminium frame parts. Some of them can be seen in **Fig. 4** and **Fig. 5**. The elbow pitch servo was attached directly under the shoulder pitch servo for reducing the inertia, using a lever mechanism for transmitting the motion to the elbow support frame, as it can be seen in **Fig. 5**. Other transmission mechanisms like timing belts were avoided due to their drawbacks in terms of backlash and complexity in the assembly. The idea of placing the actuator at the top of the link is also applied to the wrist roll joint, which can be identified as the first joint in the human forearm. Its rotation

is transmitted to the wrist pitch servo through a 140×8 mm hollow circular profile section. This frame can be used for supporting the actuators of a tendon-driven hand as done in [34] or in [35].

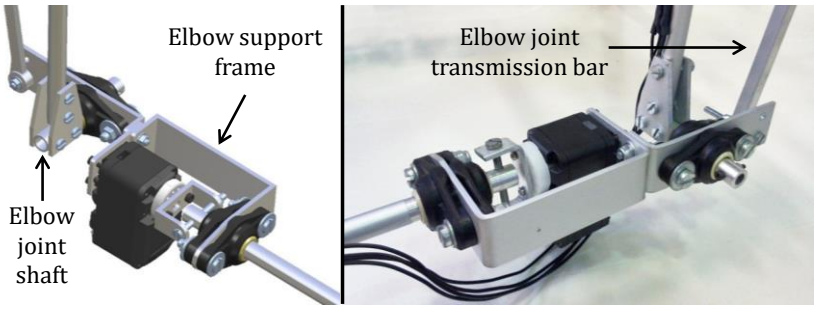

Fig. 4. Detailed view of the elbow joint mechanism and the wrist yaw servo. Radial loads exerted at the end effector are catch by the pair of igubal EFOM-08 bearings and supported by the aluminium frames.

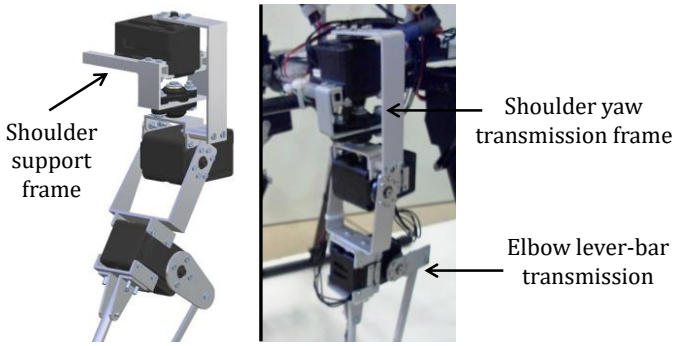

Fig. 5. Detailed view of the shoulder and upper arm assembly, including the shoulder yaw and pitch servos, and the elbow pitch servo with the lever-bar transmission mechanism for moving the elbow joint.

The assembly of both arms is done through a pair of 260×8×8 mm square hollow profiles connecting the two shoulder yaw servos as illustrated in **Fig. 6**, fixing all the parts to the servos case for maintaining the rigidity. These two square bars will be attached to the multi-rotor base under the propellers, as it can be seen in **Fig. 1**. The separation between the arms was set to 35 cm, taking into account the dimensions of the landing gear and the structure of the base where the dual arm manipulator is attached.

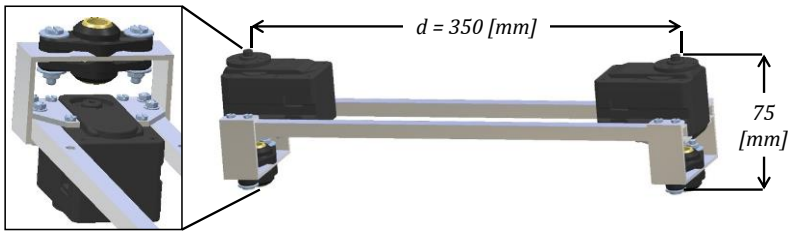

Fig. 6. General and detailed view of the shoulder structure supporting the dual arm manipulator.

3. Dual arm aerial manipulation system

3.1. Aerial platform

The developed dual arm manipulator was integrated and tested with two multirotor platforms (**Fig. 1**): a Matrice 600 hexarotor manufactured by DJI, and a customized hexarotor designed in our lab and manufactured by DroneTools. The main features of both platforms and the arms are listed in **Table 3**. As mentioned before, one of the aims of this work is contributing to bring the aerial manipulation technology to the customer applications, showing how a lightweight dual arm system specifically designed for this purpose can be integrated in a commercial multirotor platform. In general, the most relevant requirements in the choice of a multirotor intended to aerial manipulation applications are the payload and flight time, which determine the size and weight of the platform. Then, the designer has to deal with the separation

between the legs of the landing gear and the way of coupling the manipulator and other components (computer board, sensors, additional batteries, communication devices) to the frame structure of the multirotor, taking into account the motion constraints associated to the landing gear. What is more, the arms should rest above the floor plane before the take-off and landing operations to prevent undesired collisions.

Table 3. Specifications of the aerial manipulation system. Comparison of the DJI and Drone Tools hexarotor platforms.

	MULTIROTOR DJI Matrice 600	Drone Tools	DUAL ARM MANIPULATOR	
Weight (no arms)	9,1 kg	10,8 kg	Weight	1,8 kg
Tip-toTip × Height	1,65 × 0,65 m	1,7 m × 0,55 m	Max. lift load	0,75 kg
Max. lift load	8 kg	8 kg	Arms separation	0,35 m
Propellers	8 × 16”	7,3 × 21,5”	Max. joint speed	360 deg/s
LiPo Battery	6S, 6 × 4.500 mAh	6S, 16.000 mAh	LiPo Battery	3S, 4.500 mAh
Max. flight time	16 min @6 kg	20 min @8 kg	Operation time	1 hour

The mechanical integration of the developed dual arm system in the mentioned platforms is detailed in **Fig. 7** and **Fig. 8**. As it can be seen, two different solutions were adopted: attaching the arms to the two carbon fibre bars under the central hub (DJI Matrice 600, **Fig. 7**), and attaching the shoulder structure to a transversal bar disposed between the legs of the landing gear (customized hexarotor, **Fig. 8**). Note that the first configuration is more convenient in terms of dynamic coupling, as the mass of the arms is closer to the center of gravity of the multirotor, whereas in the second case the workspace of the manipulator is less affected by the landing gear and there is more space left for integrating other devices. Both platforms use the DJI A3 industrial autopilot, showing a good performance in terms of positioning accuracy despite the controller had no feedback from the arms during the flight tests (see video of the experiments in [44]).

Fig. 7. Three views of the dual arm aerial manipulation system integrated in the DJI Matrice 600 hexarotor.

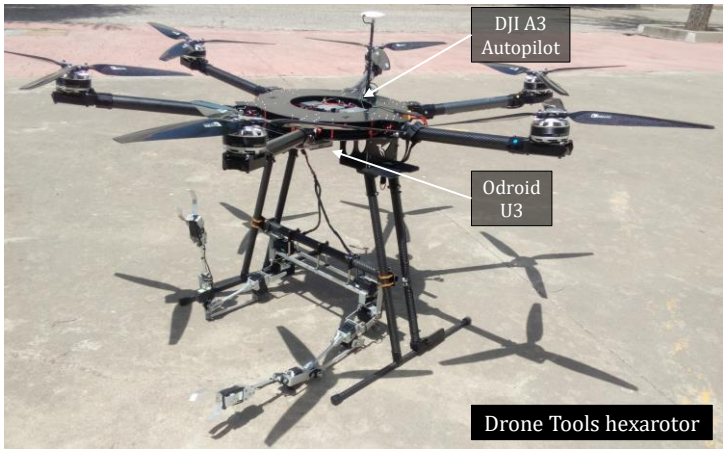

Fig. 8. Lightweight dual arm manipulator integrated in the customized hexarotor manufactured by Drone Tools.

3.2. Workspace and motion constraints

The workspace of the developed manipulator is determined by the shoulder and elbow joints. Let us consider the transversal section on the XZ plane shown in **Fig. 9**. As it can be seen, the area covered by the wrist point corresponds to a circular ring whose outer and inner limits are reached when the arm is fully stretched and retracted, respectively. The revolution of this section around the shoulder yaw axis generates a hollow semi-sphere whose volume, without considering any constraint, is $V_{arm} = 0.255\ [m^3]$.

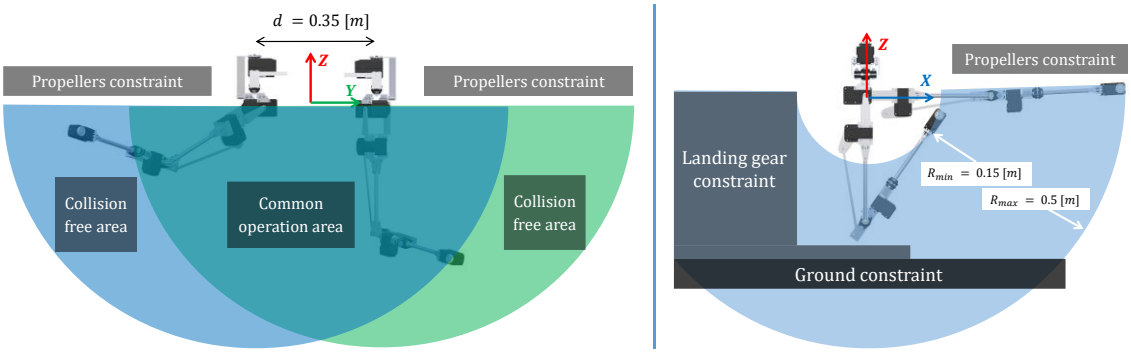

Fig. 9. Workspace covered by the shoulder pitch and the elbow pitch joints with collision constraints (left). Working space of the dual arm system with collision constraints and common operation area (right).

There are two relevant considerations related to the landing gear that can be easily inferred from the left side of **Fig. 7**. First of all, it is critical that the arms rest in a position with the forearms above the floor before the UAV lands. Otherwise, the aerial platform will suffer a collision and the arms might result damaged. This corresponds to the shaded rectangle denoted as ground constraint in **Fig. 9**. A possible solution for reducing the effect of potential accidents is introducing a mechanical fuse in the elbow joint transmission bar in such a way that this bar breaks when the forearm suffers a strong impact. The second consideration is related with the motion of the arms on flight, as it is necessary to plan carefully the trajectories to avoid collisions with the landing gear, but also with the arms themselves.

3.3. Hardware/Software Architecture

The components and architecture of the developed dual arm aerial manipulator are depicted in **Fig. 10**. The aerial platform comprises the hexarotor and the DJI A3 autopilot, which provides two flight modes: attitude stabilize, and position control. The manipulator consists of two groups of Herkulex servos, one for each arm, connected in daisy chain to the same TTL bus which ends in a USB-to-USART interface. Each servo is identified by a unique ID so the control program can access individually each actuator for reading its state and for commanding its position. Two types of data packets are transmitted through the bus. Request packets are sent from the computer board to a particular servo for commanding its position and for indicating which registers are going to be read. The response packets return the latest value of the specified registers, including the position, speed, PWM, temperature or voltage. All the servos are fed by a 3S LiPo battery, deriving a power line for feeding the computer board through a Recom 5V 1.5 A voltage regulator. The Odroid U3 computer board (with LUbuntu 13.04 OS) executes the C/C++ program that controls the arms and generates the data log files, interfacing with the servos through two USB ports. The main software component is the Task Manager, which implements the different functionalities of the arms (go to rest/operation position, teleoperation, visual servoing…) and maintains the state of the servos updated through the Arm State Threads. The arm controller implements the inverse kinematics and the trajectory generation method described in Section 5.2. Two additional sensors were integrated in the DJI Matrice 600 platform (**Fig. 7**): a ZED stereo camera intended to provide visual feedback at low frame rate to the ground control station (GCS), and a STM32F3 Discovery board used as external IMU for logging the attitude measurements. The GCS includes a display for monitoring the state of the aerial manipulator, a user interface for selecting the task to execute, and a Keep Alive Generator safety module that sends messages at 2 Hz so the Task Manager can detect communication loss and the robot can go to a safe state if necessary. The Odroid U3 is accessed through a SSH session, using UDP sockets for data interchange.

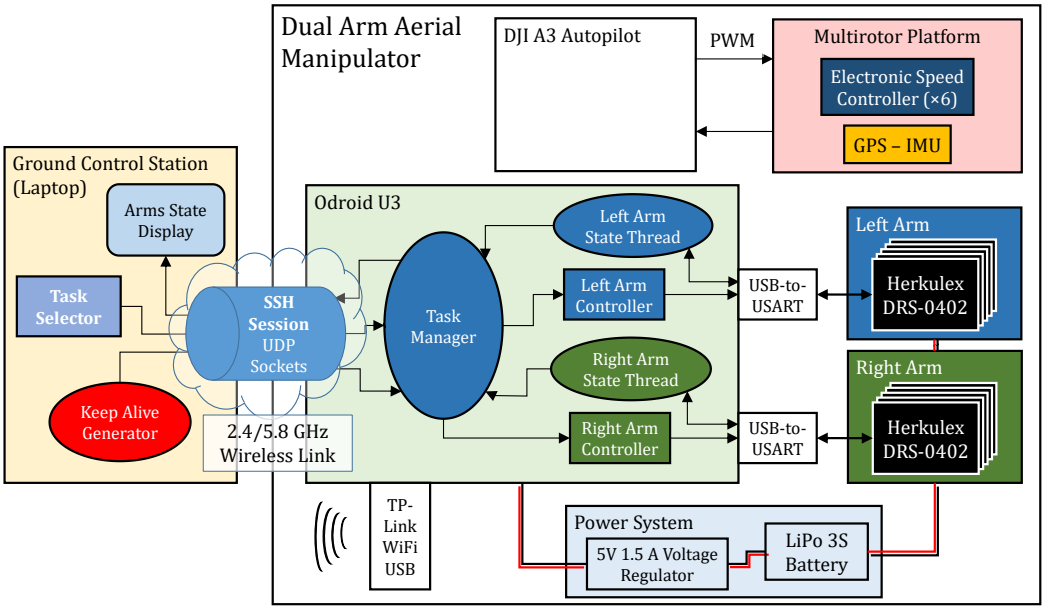

Fig. 10. Hardware/software components and architecture of the developed dual arm aerial manipulator.

4. Modelling

The kinematic and dynamic equations for the dual arm aerial manipulation system are presented here. Although the model described in this work corresponds to the dual arm case, the followed approach based on barycentric vectors can be applied to an aerial manipulator with an arbitrary number of robotic arms.

The notation employed in the equations of the kinematic and dynamic models is summarized below:

- $M = 2$: number of robot manipulators integrated in the aerial platform
- $N = 3$: number of links for each arm (only for end-effector positioning)
- $D = 12$: total number of degrees of freedom of the dual arm aerial manipulation system
- i: sub-index associated to each manipulator
- k: sub-index associated to each joint
- M_T: total mass of the dual arm aerial manipulation system
- m_k^i: mass of the k-th link of the i-th manipulator
- $\{\boldsymbol{O}\}$: inertial reference frame
- $\boldsymbol{r_M} \in \mathbb{R}^3$: position of the center of mass (CM) of the multirotor w.r.t. $\{\boldsymbol{O}\}$
- $\boldsymbol{r_{cm}} \in \mathbb{R}^3$: position of the CM of the whole system w.r.t. $\{\boldsymbol{O}\}$
- $\boldsymbol{\eta} = [\phi, \theta, \psi]^T \in \mathbb{R}^3$: roll, pitch and yaw angles representing multirotor orientation
- $\boldsymbol{q_i} = \left[q_1^i, q_2^i, q_3^i\right]^T \in \mathbb{R}^3$: shoulder yaw, pitch and elbow pitch joints for the i-th manipulator
- $\boldsymbol{\xi} = \left[\boldsymbol{r_{cm}^T}, \boldsymbol{\eta^T}, \boldsymbol{q_1^T}, \boldsymbol{q_2^T}\right]^T \in \mathbb{R}^D$: vector of generalized coordinates

4.1. Kinematic model

In the derivation of the kinematic and dynamic equations of a multirotor equipped with multiple robotic arms, it results convenient to express the position of the masses in terms of a set of body-fixed barycentric vectors [35][37]. With this, the equations of motion can be written in terms of the translation of the system center of mass (CM) with respect to an inertial reference frame.

Let consider the schematic representation of the multi-rotor platform equipped with two manipulators depicted in **Fig. 11**. The position of the CM and the attitude of the multi-rotor with respect to the inertial reference frame $\{\boldsymbol{O}\}$ are denoted by $\boldsymbol{r_M}$ and by the roll, pitch and yaw angles (ϕ, θ and ψ, respectively), while $\boldsymbol{r_{cm}}$ is the position of the CM of the whole system. Each of the $M = 2$ arms consists of $N = 3$ links

for end effector positioning, being q_k^i the k-th joint position of the i-th arm, and l_k^i and $\boldsymbol{r_k^i}$ the length and position of the CM of the respective link. The two additional DOF's provided by each arm for wrist orientation are not considered for simplicity and because they do not have a significant influence over multirotor dynamics. Taking into account the 6 DOF's for the position and attitude of the aerial platform, the total number of degrees of freedom of the system is $D = 12$.

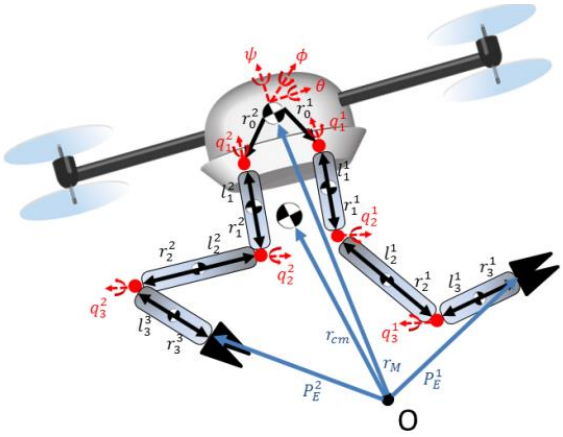

Fig. 11. Scheme of multi-rotor equipped with two 3-DOF arms.

Now it is necessary to relate the position of the CM of each single link with the position of the global CM. Let call $\boldsymbol{P_{k,a}^i} \in \mathbb{R}^3$ to the position of an arbitrary point a on the link k of the manipulator i given by:

$$\boldsymbol{P_{k,a}^i} = \boldsymbol{r_{cm}} + \boldsymbol{\rho_k^i} + \boldsymbol{r_{k,a}^i} \tag{2}$$

where $\boldsymbol{r_{k,a}^i} \in \mathbb{R}^3$ is the position vector from the k-th link CM of manipulator i to point a, and $\boldsymbol{\rho_k^i} \in \mathbb{R}^3$ is computed in the following way:

$$\boldsymbol{\rho_k^i} = \boldsymbol{T_0} \sum_{p=1}^{M} \sum_{j=1}^{N} \boldsymbol{R_{0,j}^p} \cdot \boldsymbol{v_{j(k\delta_{ip})}^p} \tag{3}$$

Here δ_{ip} is the Kronecker delta, $\boldsymbol{T_0} \in \mathbb{R}^{3\times3}$ is the rotation matrix of the multirotor with respect to the inertial frame, and $\boldsymbol{R_{0,j}^p} \in \mathbb{R}^{3\times3}$ is the rotation matrix between the j-th link frame of manipulator p and the frame of the aerial platform. Taken into account Equation (3), Equation (2) can be rewritten as:

$$\boldsymbol{P_{k,a}^i} = \boldsymbol{r_{cm}} + \boldsymbol{\rho_k^i} + \boldsymbol{r_{k,a}^i} = \boldsymbol{r_{cm}} + \boldsymbol{T_0} \sum_{p=1}^{M} \sum_{j=0}^{N} \boldsymbol{R_{0,j}^p} \cdot \boldsymbol{v_{jk,a}^p} \tag{4}$$

$$\boldsymbol{v_{jk,a}^i} = \boldsymbol{v_{jk}^i} + \delta_{ja}^i \cdot \boldsymbol{r_{k,a}^i} \tag{5}$$

where $\boldsymbol{v_{jk}^i} \in \mathbb{R}^3$ is the barycentric vector defined as the position vector of the k-th link CM of manipulator i-th w.r.t. the system CM:

$$\boldsymbol{v_{jk}^i} = \begin{cases} r_j^{i*} = -l_j^i \mu_j^i + r_j^i \mu_{j+1}^i & j < k \\ c_j^{i*} = -l_j^i \mu_j^i - r_j^i (1 - \mu_{j+1}^i) & j = k \\ l_j^{i*} = l_j^i (1 - \mu_j^i) - r_j^i (1 - \mu_{j+1}^i) & j > k \end{cases} \tag{6}$$

where $l_j^i \in \mathbb{R}^3$ and $\boldsymbol{r_j^i} \in \mathbb{R}^3$ are defined in **Fig. 11** and the mass distribution, μ_j^i, is given by:

$$\mu_j^i = \begin{cases} 0 & j = 0 \\ \dfrac{m_0}{M_T} + \displaystyle\sum_{p=1}^{M} \sum_{k=1}^{N(i,j,p)} \dfrac{m_k^p}{M_T} & j = 1, \dots, N \\ 1 & j = N+1 \end{cases} \tag{7}$$

$$N(i,j,p) = N - \delta_{ip}(N - j + 1) \tag{8}$$

Note from Equation (7) that the position of the CM of each link respect to the inertial frame depends on the position of all links. The system center of mass is then computed as follows:

$$\boldsymbol{r_{cm}} = \frac{1}{M_T}\left(\boldsymbol{r_M} m_0 + \sum_{i=1}^{M} \sum_{j=1}^{N} \boldsymbol{d_j^i} \cdot m_j^i \right) \tag{9}$$

$$\boldsymbol{d_j^i} = \boldsymbol{r_M} + \boldsymbol{T_0} \sum_{p=1}^{j} (\boldsymbol{R_{0,p-1}^i} \cdot \boldsymbol{r_{p-1}^i} - \boldsymbol{R_{0,p}^i} \cdot \boldsymbol{l_p^i}) \tag{10}$$

The position of the end effector for each manipulator is obtained from Equation (4):

$$\boldsymbol{P_E^i} = \boldsymbol{r_{cm}} + \boldsymbol{T_0} \sum_{p=1}^{M} \sum_{j=1}^{N} \boldsymbol{R_{0,j}^p} \cdot \boldsymbol{v_{jN,E}^p} \tag{11}$$

where $\boldsymbol{r_M}$ represents the multirotor center of mass position with respect to the inertial frame and $\boldsymbol{R_{0,0}^i}$ is the identity matrix. Using Equations (6) - (8), it results that:

$$\boldsymbol{P_E^i} = \begin{pmatrix} r_{Mx}^i \\ r_{My}^i \\ r_{Mz}^i \end{pmatrix} + \boldsymbol{T_0} \begin{pmatrix} r_{0x}^i + rl_1^i C_{q_1^i}\left(rl_2^i S_{q_2^i} + rl_3^i S_{q_{2,3}^i} \right) \\ r_{0y}^i + rl_1^i S_{q_1^i}\left(rl_2^i S_{q_2^i} + rl_3^i S_{q_{2,3}^i} \right) \\ r_{0z}^i - rl_1^i - rl_2^i C_{q_2^i} - rl_3^i C_{q_{2,3}^i} \end{pmatrix} \tag{12}$$

with $rl_j^i = \left(r_j^i - l_j^i\right)$, $C_{q_j^i} = cos(q_j^i)$, $S_{q_j^i} = sin(q_j^i)$, $C_{q_{j,k}^i} = cos(q_j^i + q_k^i)$, and $S_{q_{j,k}^i} = sin(q_j^i + q_k^i)$. Equations (3) and (4) can be differentiated with respect to the time to obtain the position velocity of an arbitrary point a in the body k of the i-*th* manipulator:

$$\dot{\boldsymbol{P}}_{\boldsymbol{k,a}}^{\boldsymbol{i}} = \dot{\boldsymbol{r}}_{\boldsymbol{cm}} + \dot{\boldsymbol{\rho}}_{\boldsymbol{k}}^{\boldsymbol{i}} + \dot{\boldsymbol{r}}_{\boldsymbol{k,a}}^{\boldsymbol{i}} \tag{13}$$

$$\dot{\boldsymbol{\rho}}_{\boldsymbol{k}}^{\boldsymbol{i}} = \sum_{p=1}^{M} \sum_{j=0}^{N} \boldsymbol{\omega_j^p} \times \boldsymbol{v}_{\boldsymbol{j(k\delta_{ip})}}^{\boldsymbol{p}} \in \mathbb{R}^3 \tag{14}$$

$$\boldsymbol{\omega_k^i} = \boldsymbol{\omega_0} + \boldsymbol{T_0} \cdot \boldsymbol{T_k^i} \cdot \dot{\boldsymbol{q}}^{\boldsymbol{i}} \in \mathbb{R}^3 \tag{15}$$

$$T_k^i = \left[R_{0,1}^i u_1^i, R_{0,2}^i u_2^i, \dots, R_{0,k}^i u_k^i, 0, \dots, 0 \right] \in \mathbb{R}^{3\times 3} \tag{16}$$

with $\omega_0^p = \omega_0$ $(p = 1, \dots, M)$ denoting the multirotor angular velocity with respect to the inertial frame and vector $\dot{\boldsymbol{q}}^{\boldsymbol{i}} = \left[q_1^i \; q_2^i \; q_3^i \right]^T \in \mathbb{R}^N$ represents the joint rates of the i-th manipulator. The terms $u_j^i \in \mathbb{R}^3$ $(i = 1, \dots, M, j = 1, \dots k)$ are unit column vectors and represent the rotation axis of the j-th joint of the i-th manipulator.

4.2. Dynamic model

The dynamic model of the dual arm aerial manipulation system is derived from the Lagrangian and the well-known Euler-Lagrange equation:

$$\frac{d}{dt}\left\{\frac{\partial L}{\partial \dot{\boldsymbol{\xi}}}\right\} - \frac{\partial L}{\partial \boldsymbol{\xi}} = \boldsymbol{\Gamma} \tag{17}$$

$$L(\boldsymbol{\xi}, \dot{\boldsymbol{\xi}}) = K(\boldsymbol{\xi}, \dot{\boldsymbol{\xi}}) - V(\boldsymbol{\xi}) \tag{18}$$

where L is the Lagrangian, defined as the difference between the kinetic and the potential energy of the system, K and V, respectively, $\boldsymbol{\Gamma}$ is the vector of generalized forces and torques, and $\boldsymbol{\xi}$ is the vector of generalized coordinates. This vector includes the position of the CM of the multirotor and its attitude, along with the joint positions of both manipulators:

$$\boldsymbol{\xi} = \left[\boldsymbol{r_{cm}^T}, \boldsymbol{\eta}^T, \boldsymbol{q_1^T}, \boldsymbol{q_2^T}\right]^T \in \mathbb{R}^D \tag{19}$$

Here $\boldsymbol{r_{cm}} = [x_{cm}, y_{cm}, z_{cm}]^T \in \mathbb{R}^3$, $\boldsymbol{\eta} = [\phi, \theta, \psi]^T \in \mathbb{R}^3$ represents vehicle attitude by means of the roll, pitch, yaw Euler angles, while $\boldsymbol{q_i} = \left[q_1^i, q_2^i, q_3^i\right]^T$ is the joint position vector for the i-th manipulator. The system can be considered as a kinematic tree where the multirotor is connected to a fixed base via a 6-DOF joint and each robot manipulator is a subtree connected to the multirotor, being the kinetic energy of the tree equal to the sum of the kinetic energies of its bodies. The benefit of using the barycentric vectors (Equation (6)) is that the manipulators can be replaced by virtual manipulators whose base is the system CM. Therefore, the kinetic energy of the system is given by:

$$T = \frac{1}{2} M_T \dot{\boldsymbol{r}}_{\boldsymbol{cm}}^{\boldsymbol{T}} \dot{\boldsymbol{r}}_{\boldsymbol{cm}} + \frac{1}{2} \sum_{i=1}^{M} \sum_{k=1}^{N} \{\omega_k^i \, I_k^i \omega_k^i + m_k^i \, \dot{\rho}_k^i \dot{\rho}_k^i\} \tag{20}$$

In this equation, the first term corresponds to the kinetic energy associated to the translational speed of the system, while the two terms within the nested summation are the kinetic energy due to the translation and rotation of the link masses, being ω_k^i the rotational speed of the k-th joint in the i-th manipulator. The potential energy due to gravity can be calculated with respect to the system center of mass as:

$$V = g M_T z_{cm} \tag{21}$$

where g is the acceleration due to gravity and z_{cm} is the altitude of the center of mass (see Equation (9)). The equation of motion of the system can be expressed in the following general form:

$$\boldsymbol{M}(\boldsymbol{r})\ddot{\boldsymbol{\xi}} + \boldsymbol{C}(\boldsymbol{r}, \dot{\boldsymbol{r}})\dot{\boldsymbol{\xi}} + \boldsymbol{G}(\boldsymbol{\xi}) = \boldsymbol{\Gamma} \tag{22}$$

Here $\boldsymbol{M} \in \mathbb{R}^{D \times D}$, $\boldsymbol{C} \in \mathbb{R}^D$ and $\boldsymbol{G} \in \mathbb{R}^D$ are respectively the inertia matrix, the centrifugal and Coriolis terms, and the gravitational force term. The vector $\boldsymbol{r} = [\boldsymbol{\eta}, \boldsymbol{q^1}, \boldsymbol{q^2}]^T$ represents the multirotor rotation and the manipulators' joint angles. The inertia matrix resulting for the developed dual arm aerial manipulation system has the following form:

$$\boldsymbol{M}(\boldsymbol{r}) = \begin{bmatrix} \boldsymbol{I}_{3\times3} M_T & \boldsymbol{0}_{1\times3} & \boldsymbol{0}_{1\times3} & \boldsymbol{0}_{1\times3} \\ \boldsymbol{0}_{3\times1} & \boldsymbol{M_\eta}(\boldsymbol{r}) & \boldsymbol{M_{\eta q1}}(\boldsymbol{r}) & \boldsymbol{M_{\eta q2}}(\boldsymbol{r}) \\ \boldsymbol{0}_{3\times1} & \boldsymbol{M_{\eta q1}^T}(\boldsymbol{r}) & \boldsymbol{M_{q1}}(\boldsymbol{r}) & \boldsymbol{M_{q1q2}}(\boldsymbol{r}) \\ \boldsymbol{0}_{3\times3} & \boldsymbol{M_{\eta q2}^T}(\boldsymbol{r}) & \boldsymbol{M_{q1q2}^T}(\boldsymbol{r}) & \boldsymbol{M_{q2}}(\boldsymbol{r}) \end{bmatrix} \tag{23}$$

where $I_3 \in \mathbb{R}^{3\times3}$ is the identity matrix. It is interesting to note in the form of this matrix the decoupling between the translation and rotation of the aerial manipulation system.

4.3. Interactions between the manipulator and the aerial platform

The terms $\boldsymbol{M_{\eta q1}}$ and $\boldsymbol{M_{\eta q2}}$ in Equation (23) are the submatrices of inertia, which represent the dynamic coupling between the multirotor and the arms. The structure of the inertia matrix is derived from the application of the method of barycentric vectors in the calculation of the kinematic and dynamic equations, referenced to the center of mass of the whole aerial manipulator. This fact is evidenced by the null term in the cross-submatrices where the acceleration of the center of mass (linear and twist) are related. The main benefit of this method is that the equations obtained result in a more compact and simple form for its implementation in a simulation framework, and for the design of a model-based controller. The drawback is that the observation of the dynamic effects associated to the interactions between the arms and the aerial platform requires the transformation to the kinematic domain.

A MATLAB/Simulink simulator was developed for identifying the reaction torques introduced in the base of the aerial platform due to the motion of the arms, obtaining the dynamic/kinematic equations using the MUPAD toolbox of MATLAB. **Fig. 12** shows the inertia, Coriolis and gravity components of the torque in the three axis when the left arm rotates from 0 to 90 degree in one second time. This estimation is obtained from the application of the dynamic model over the data provided by the servo actuators in the physical manipulator.

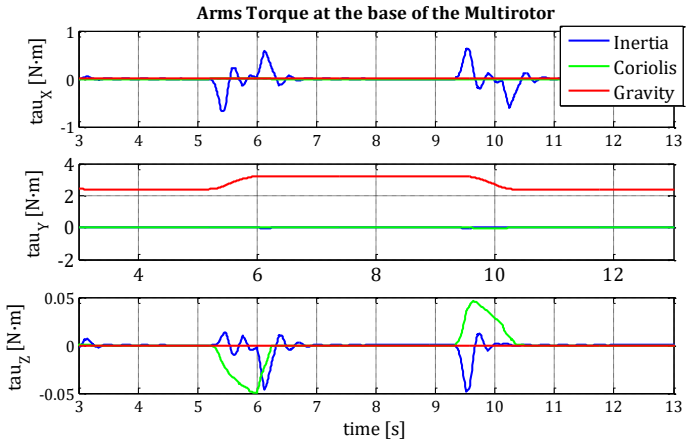

Fig. 12. Inertia (blue), Coriolis and centrifugal (green) and gravity (red) terms in the XY axes for the 90 deg step in the shoulder pitch joint of the left arm. The components in the X and Z axes are caused by the asymmetry in the motion of the arms.

This example demonstrates that the gravity term is dominant in the pitch angle, whereas the inertia and Coriolis terms in the roll and yaw angles are associated to the unbalanced motion of the masses, as there is no compensation with the right arm. What is more, the offset component in the gravity term represents the displacement of the center of mass when the arms are attached to the aerial platform, and it should be compensated by the integral term in the autopilot during the flight operation.

The dynamic model described in Section 4.2 shows a strong coupling between the manipulator and the multirotor, in such a way that the acceleration of any link in one arm will affect, not only to the aerial platform, but also to the joint torque in the other arm. Nevertheless, the torque induced in the joints by the acceleration of the aerial platform will be in practice dissipated by the relative high friction of the gearbox of the servos, and by the embedded position controller. In other words, the motion of the arms will affect the stability of the aerial platform, but the opposite effect is not significant.

5. Control

Most model-based controllers assume that joint torque control or feedback is possible. However, the servo actuators typically employed for building low weight robotic arms intended to aerial manipulation only provide position measurements at low rates (<100 Hz). What is more, the controller embedded in these

devices only accepts motion commands specifying the desired goal position and playtime. These technological limitations have motivated the design of the control scheme described in this section.

5.1. Structure of the controller

Let consider an aerial manipulation task in which the arms should execute a certain operation on flight while the aerial platform remains stable in hover. It is assumed that arms can move independently while the aerial platform remains in hover. In order to compensate positioning and orientation disturbances due to dynamic coupling, the controller will compensate the reaction torques that the arms exert over base of the UAV. This scheme is represented in **Fig. 13**. The dual arm aerial manipulator consists of the aerial platform with the left and right arms. The task manager module generates the desired UAV and arms trajectories for accomplishing the specific task, keeping updated the current state of the robot. A torque estimator is developed, taking as input the joints position and speed of the arms, giving as output the estimated reaction torque of the arms computed from the dynamic model presented in Section 4.2. A Phase Lock Loop (PLL) provides smooth estimations of joint acceleration from the speed of each servo, avoiding errors associated to the differentiation of the speed signal. The UAV controller takes as input the data provided by the Inertial Measurement Unit (IMU) along with the arms torque estimation for the compensation (see Section 4.3.3), and the reference trajectory generated by the task manager, giving at its output the control signal $\boldsymbol{U} = \left[u_z, u_\phi, u_\theta, u_\psi\right]^T$ for the total thrust and the roll, pitch and yaw torque inputs of the multirotor. The controller of the arms, detailed in Section 4.3.2, takes as input the desired Cartesian trajectory of the Tool Center Point (TCP) and the state of the servos, providing the references for each servo in the arms.

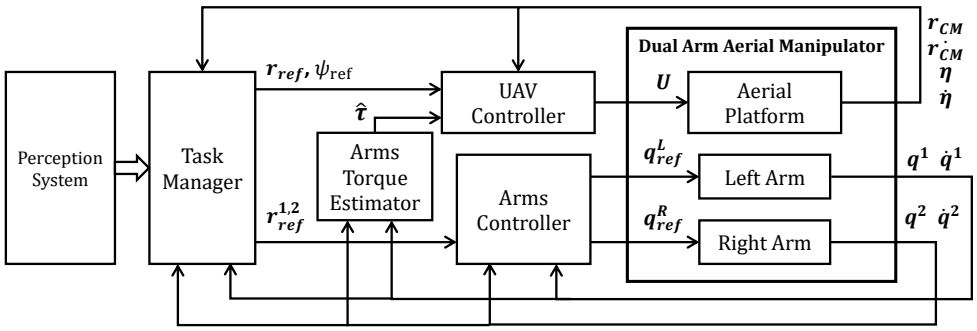

Fig. 13. Control structure for the dual arm aerial manipulator with arms torque compensation.

The proof of stability of the position/attitude controller with torque compensation is out of the scope of this work. However, intuitively, the performance of the controller will be qualitatively improved if the arms torque estimation is accurate enough and the delay in the signal transmission and processing is at least five times lower than the lowest time constant of the system. Note that the natural frequency in the attitude control of a high inertia mechanical system as a multirotor is around 1 – 2 Hz, whereas the update rate of the torque estimator is 50 Hz.

5.2. Arms controller

A simple trajectory generation method that exploits the position controller embedded in the Herkulex servos is described here. The goal is that the end effector follows a sequence of way-points with smooth variations of the velocity profile, avoiding acceleration peaks. According to the manual of the servos [40], three working modes are defined: normal operation mode, Velocity Over-Ride (VOR) disabled, and VOR enabled. These have been illustrated in **Fig. 14**. Each servo takes as input the desired goal position and the play time, that is, the desired time for reaching the goal position. The embedded servo controller generates then a trapezoidal velocity profile for satisfying the position and timing constraints.

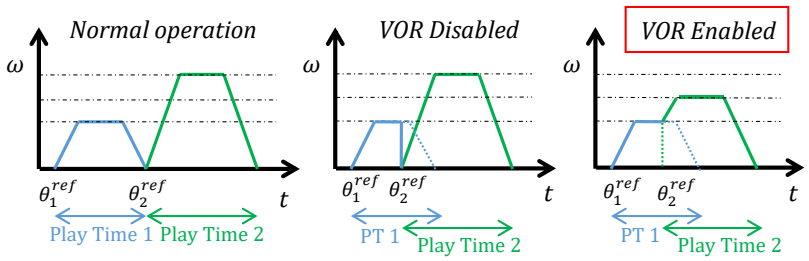

Fig. 14. Velocity profiles for the three operation modes of the Herkulex servos. In the Velocity Over-Ride (VOR) mode, the new profile (green) is re-computed from the velocity in the time instant the new reference is received, preventing acceleration peaks.

The trajectory generation method described in **Fig. 15** makes use of the VOR mode for achieving smooth motions with the manipulators. Let $\boldsymbol{P_E^i}$ be a continuous time trajectory in the Cartesian space for the end effector of the i-th manipulator, which is sampled each T seconds for obtaining the corresponding sequence of way-points. Applying the inverse kinematic model, the joint position references $q^i_{1,ref}$, $q^i_{2,ref}$ and $q^i_{3,ref}$ are obtained. Now, it is imposed that joint position references are sent to the servos at the midpoint of the velocity profile, that is, 50% of the elapsed play time, which implies that the play time is equal to $2 \cdot T$. This constraint ensures that the velocity profile is re-generated from the constant speed zone. The manual of the servos specifies that the velocity profile is symmetrical, with a default acceleration ratio of 25% of the play time. Experimental results show that the way-point sampling period T should be over 25 ms, as the internal control period for the servos is 11.3 ms. Note that this timing-based control scheme is not affected by error integration, as the error is only allow to grow during a play time period and it is reset with each new joint position reference.

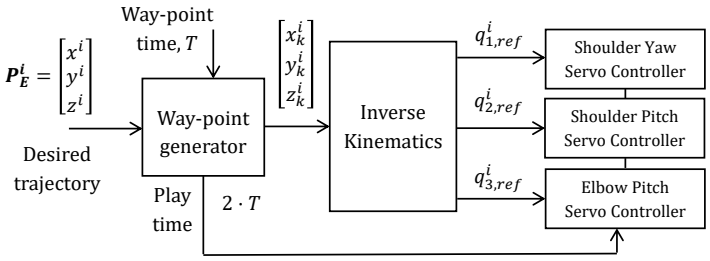

Fig. 15. Arms control structure based on inverse kinematics. Smooth trajectories are achieved sending the position references to the servos at the midpoint of the trapezoidal velocity profile, imposing that the play time is two times the way-point tracking time.

5.3. UAV controller

A nonlinear controller based on integral backstepping [40] adapted to the dual arm configuration is employed in the control scheme shown in **Fig. 13**. The attitude controller compensates the reaction torques that the arms generate over the aerial platform, using the measurement provided by the arms torque estimator for this purpose. The complete derivation of the controller can be found in [40], the expressions for the attitude controller is summarized in the following. The attitude control signals (the roll, pitch and yaw multirotor torque inputs) can be computed as:

$$\boldsymbol{U_\eta} = \begin{bmatrix} u_\phi \\ u_\theta \\ u_\psi \end{bmatrix} = \boldsymbol{M_\eta^{-1}}\left[\boldsymbol{K_1 e_\eta} + \boldsymbol{K_2 e_{\dot{\eta}}} + \boldsymbol{K_3 \chi_\eta}\right] + \boldsymbol{C_\eta} + \boldsymbol{G_\eta} + \boldsymbol{\tilde{M}_{\eta q}} \tag{24}$$

where the term $\boldsymbol{\tilde{M}_{\eta q}}$ compensates the inertia terms associated to the arms joints:

$$\boldsymbol{\tilde{M}_{\eta q}} = [\boldsymbol{M_{\eta q1}(r)} \quad \boldsymbol{M_{\eta q2}(r)}] \begin{bmatrix} \ddot{\boldsymbol{q}}^1 \\ \ddot{\boldsymbol{q}}^2 \end{bmatrix} \in \mathbb{R}^3 \tag{25}$$

and the tracking error, $\boldsymbol{e_\eta}$, its integral,$\boldsymbol{\chi_\eta}$, and the angular speed tracking error, $\boldsymbol{e_{\dot{\eta}}}$, are given by:

$$\boldsymbol{e_\eta} = \boldsymbol{\eta_d} - \boldsymbol{\eta} \in \mathbb{R}^3 \tag{26}$$

$$\boldsymbol{\chi_\eta} = \int_0^t \boldsymbol{e_\eta}(t)dt \in \mathbb{R}^3 \tag{27}$$

$$\boldsymbol{e_{\dot{\eta}}} = \boldsymbol{k_\eta e_\eta} + \boldsymbol{\lambda_\eta \chi_\eta} + \dot{\boldsymbol{\eta}}_{\boldsymbol{d}} - \dot{\boldsymbol{\eta}} \in \mathbb{R}^3 \tag{28}$$

The gains of the controller are computed in the following way:

$$\boldsymbol{K_1} = \mathbb{I}_3 - \boldsymbol{\lambda_\eta^2} + \boldsymbol{k_\eta} \in \mathbb{R}^{3\times3} \tag{29}$$

$$\boldsymbol{K_2} = \boldsymbol{k_\eta} + \boldsymbol{k_{\dot{\eta}}} \in \mathbb{R}^{3\times3} \tag{30}$$

$$\boldsymbol{K_3} = -\boldsymbol{k_\eta \lambda_\eta} \in \mathbb{R}^{3\times3} \tag{31}$$

Here $\mathbf{k_\eta}$, $\mathbf{k_{\dot{\eta}}}$ and $\boldsymbol{\lambda_\eta}$ are positive diagonal gain matrices of the controller. The vectors $\boldsymbol{C_\eta} \in \mathbb{R}^3$ and $\boldsymbol{G_\eta} \in \mathbb{R}^3$ are the lower part of the Coriolis and centrifugal force and gravity force vectors, respectively. A detailed description of the backstepping controller can be found in [40].

5.4. Arms torque estimator

The control method described in Section 5.1 and represented in **Fig. 13** relies on the estimation of the reaction torques caused by the motion of the arms, which are introduced in the base of the aerial platform. This approach exploits the knowledge on the dynamics of the system (see Section 4.2), considering that the reaction of the arms over the multirotor can be computed and thus compensated by the attitude controller. Unlike the problem of estimating and controlling a multirotor vehicle affected by external wrenches [22] [23] like wind disturbances or unknown contact forces, the compensation of endogenous forces/torques is a more simple problem in the sense that its estimation is straightforward if the state of the servos is known and the dynamic model is available.

The structure of the Arms Torque Estimator block of **Fig. 13** is detailed in **Fig. 16**. The servo actuators provide joint position and speed measurements at 50 Hz, obtaining the acceleration signal at the output of a Phase Lock Loop (PLL). This method is preferred to the differentiation as it provides smoother estimations and attenuates the effect of noise and outliers in the velocity signal. The position, velocity and acceleration of the shoulder and elbow joint servos is then provided to the dynamic model, giving as output the gravity, centrifugal and Coriolis terms, and the inertia torque components referred to the system center of mass. These were identified in the experiment shown in **Fig. 12**.

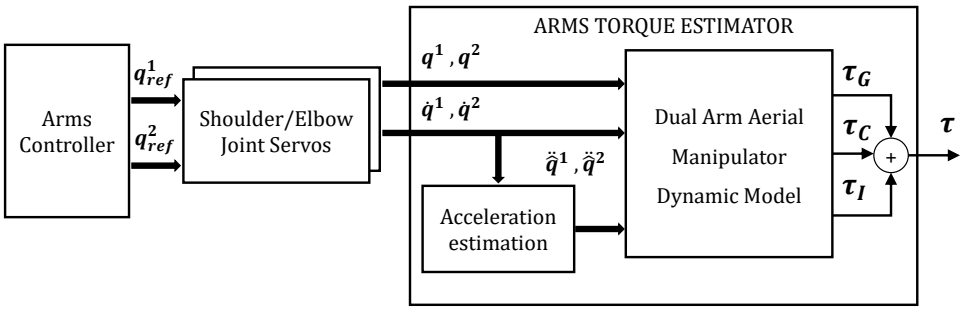

Fig. 16. Detailed view of the arms torque estimator.

6. Experimental results

Three types of experiments have been conducted for evaluating the performance of the lightweight dual arm manipulator. The trajectory generation method described on Section 4.3 is applied for tracking a circular trajectory and for visual servoing. The possibility of compensating the reaction torques in the roll

and yaw angles coordinating the motion of the left and right arms is evaluated in test-bench. Finally, the low weight and inertia design is validated in an outdoor flight test, generating different motion sequences with the arms while the UAV is hovering for evaluating qualitatively the effect of the dynamic coupling.

6.1. Trajectory tracking: Accuracy and Repeatability

The main purpose of this experiment is evaluating the repeatability and accuracy in the positioning of the wrist point of both arms using the control method described in Section 4.3.2. Both arms executed a 30 cm amplitude circular trajectory in the YZ plane, maintaining constant the position in the X-axis. The motion of both arms is coordinated and given by the following discrete point trajectory:

$$\begin{aligned} x(k) &= 0.2 \\ y(k) &= \pm 0.05 + 0.15 \cdot \sin(10 \cdot \pi \cdot k/N) \\ z(k) &= -0.25 + 0.15 \cdot \cos(10 \cdot \pi \cdot k/N) \end{aligned} \tag{32}$$

Here k denotes the way-point index and $N = 100$ is the number of way-points, which corresponds to five turns. A ±0.05 [m] offset term has been introduced in the Y-axis representing the separation of left and right wrist points with respect the reference trajectory. The play time for the servos was set to 0.25 s, with a jump time between way points of 0.125 s (50% of the velocity profile). **Fig. 17** represents the Cartesian trajectory followed by the wrist point for both arms derived from the forward kinematic model applied over joint position measurements. As it can be seen on the right side of **Fig. 17**, the deviation in the X-axis is under 1 cm. A modified version of the CAMShift color-based tracking algorithm [38][39] has been employed for determining the position on the image plane of a color marker attached to the wrist of both arms. **Fig. 18** shows a pair of frames captured in frontal (left) and lateral (right) view points, along with the trajectory followed by the color markers. Note that the visual tracking of the color marker introduces a certain error in the projection of the trajectory.

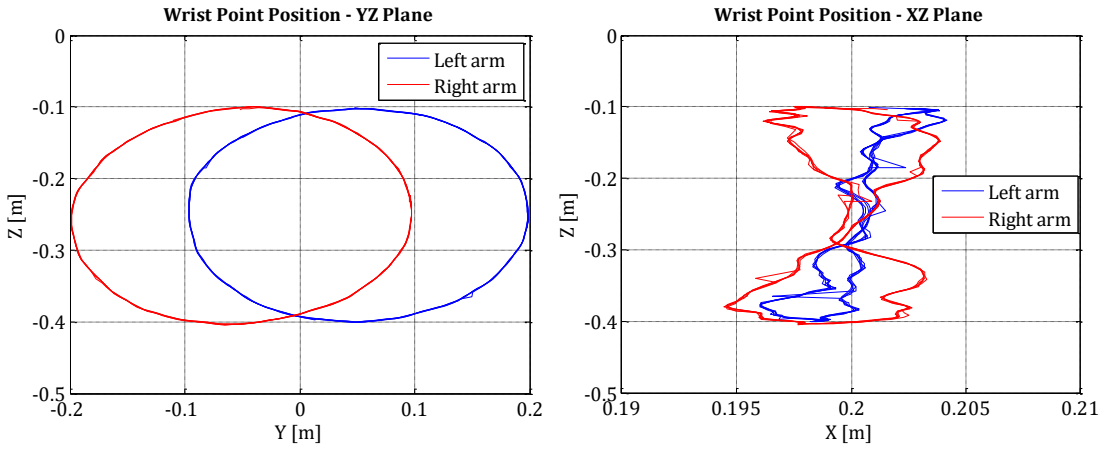

Fig. 17. Circular trajectory followed by the wrist point of left and right arms in the YZ plane (left) and XZ plane (right). The arms performed five complete turns for evaluating repeatability and accuracy. Note the scale of the X-axis on the right figure.

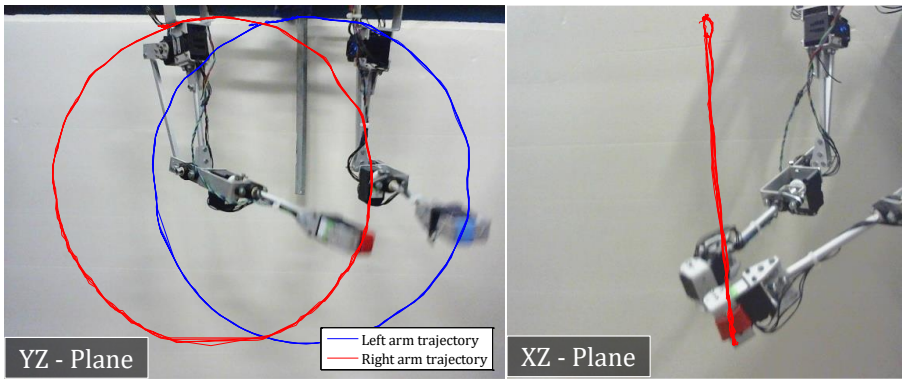

Fig. 18. Tracking points given by the CAMShift algorithm in the frontal and side planes corresponding to the circular trajectory.

6.2. Visual servoing

In this experiment, a ZED camera was attached over the shoulder structure of the arms (see **Fig. 2** left) looking 45 deg downwards so its field of view covered most part of the workspace of the manipulator. Two ARUCO [42] tags attached to an aluminium bar at 25 cm distance between them are visually tracked by the camera, providing the relative position of each tags in the arms local frame (**Fig. 3**) to the arms controller described in Section 4.3.2. The trajectories of the marker (red line), the reference Cartesian position (black) and the feedback position of the arms (blue) are represented in **Fig. 19**. The aluminium frame was rotated and translated in different axes. A separation distance of 10 cm between the wrist point and the marker was imposed for preventing the arms occluded the tags.

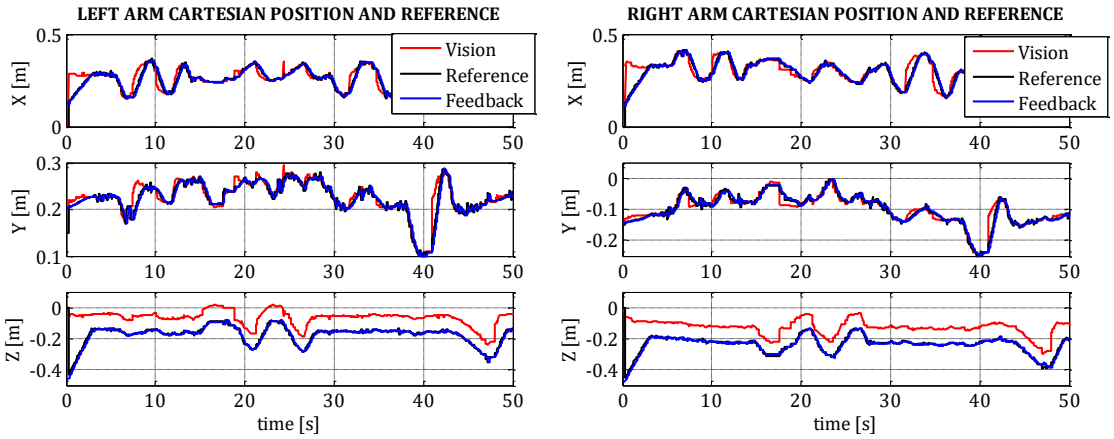

Fig. 19. Cartesian position of the left and right arms in the visual servoing experiment. Each arm tracked an ARUCO tag. An offset distance of 10 cm in the Z-axis was introduced for avoiding that the tags are occluded by the end effector.

6.3. Step response: identification of joints state

In this experiment the arms generate a sequence of rotations, 90 deg amplitude, around their joints in the following order: shoulder pitch, shoulder yaw, and elbow pitch. The complete sequence is depicted in **Fig. 20**, representing also the joint speed and acceleration, obtained at 50 Hz. The sign criteria is the one defined in **Fig. 3**. Each rotation requires one second time, waiting another second until the next movement starts. From t = 5 s to t = 15 s the arms execute a symmetric motion around the XZ plane, so the torque in the roll and yaw angles is cancelled. From t = 22 to t = 32 s only the left arm moves, generating an uncompensated reaction torque at the base of the arms.

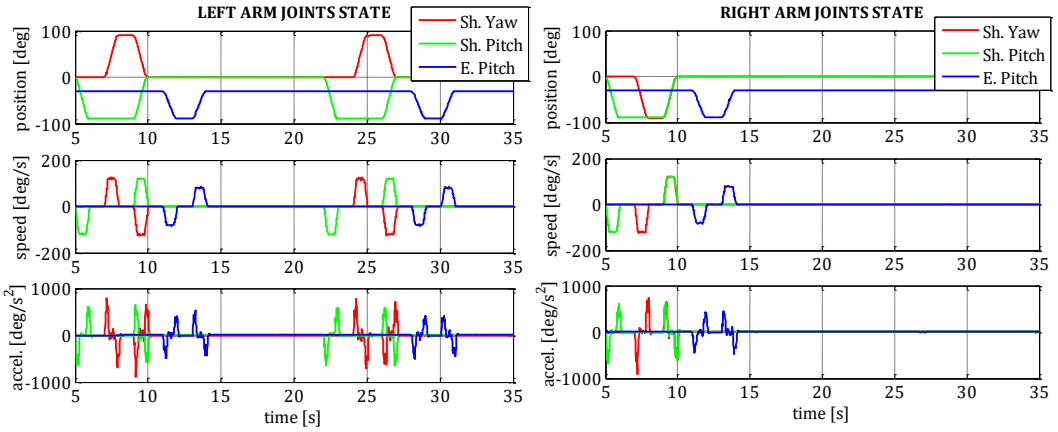

Fig. 20. Position, speed and acceleration of the shoulder yaw (red), pitch (green) and elbow pitch (blue) joints of the arms.

6.4. Dual arm – platform interactions

The physical interaction between the dual arm manipulator and the aerial platform, represented by the terms $\boldsymbol{M_{\eta q1}}$ and $\boldsymbol{M_{\eta q2}}$ in the inertia matrix defined by Equation (23), is experimentally verified here. The experiments were conducted in a test bench, hanging the aerial platform from four wires attached to the central hub so that the reaction torques caused by the motion of the arms could be appreciated more clearly. The idea was to emulate hovering conditions without the action of the autopilot, allowing the free rotation of the platform at expenses of constraining its translation. The experimental setup and the tests performed can be seen in the video attachment or in [44]. The acceleration, angular speed and magnetic field at the base of the DJI Matrice 600 platform were measured with a STM32F3 Discovery board, used as external IMU connected to the Odroid U3 computer. The arms executed a simple sequence of four rotations ($0 \rightarrow 90$ deg in q_2 | $0 \rightarrow \pm 90$ deg in q_1 | $\pm 90 \rightarrow 0$ deg in q_1 | $90 \rightarrow 0$ deg in q_2) with two different play times (1 s and 0.5 s), according to the criteria defined in **Fig. 3**. Two use cases are also considered: symmetric motion of the left/right arms w.r.t. the XZ plane, and asymmetric motion moving only the left arm. **Fig. 21** represents the servo position, speed, PWM, and the angular rate of the UAV in three cases.

The data provided by the gyroscope confirms two intuitive effects: 1) the amplitude of the oscillation of the hexarotor in the Y-axis caused by the rotation of the shoulder pitch joints is almost duplicated when the joint speed is two times higher (1st – 2nd cols), and 2) the asymmetry in the motion of the arms induces a reaction in the roll and yaw angles (3rd col) which is compensated if the trajectory of the right arm is symmetric w.r.t. the XZ plane (1st, 2nd col). However, the partial torque compensation in these two axes is achieved at expenses of increasing the reaction induced in the third axis. These effects are not so evident when the aerial manipulator is on flight due to sensor noise, wind perturbations, but especially due to the action of the autopilot, as the derivative term of the controller tends to compensate errors in angular rate.

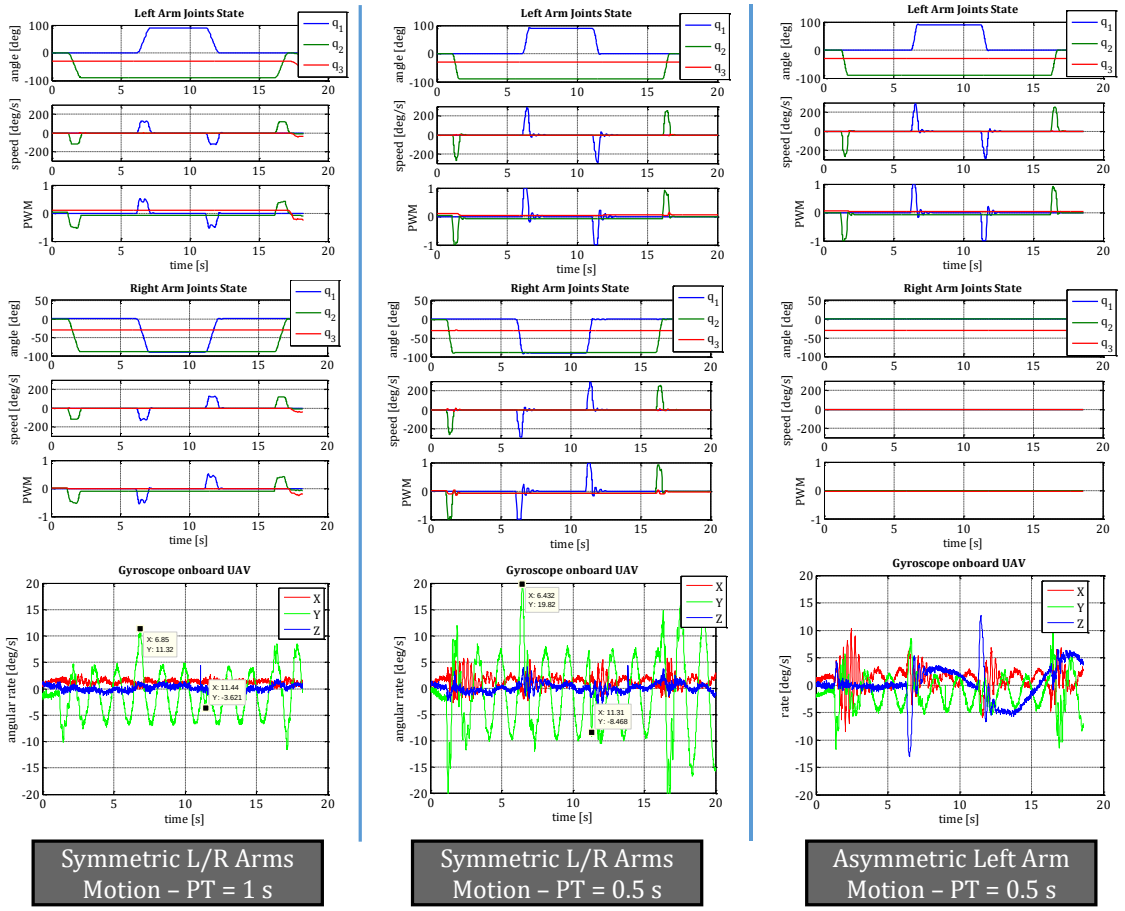

Fig. 21. Servo position, speed and PWM in the left (first row) and right (second row) arms during a sequence of rotations around the shoulder pitch and yaw joints. Oscillations in the platform are measured with a three axis gyroscope (third row). The amplitude and axes involved in the reaction of the platform depend on the joints speed and symmetry of the arms trajectory (cols 1 – 2 vs col 3).

6.5. Outdoor flight tests

An extensive set of flight tests were conducted in outdoors with the developed dual arm manipulator integrated in the DJI Matrice 600 and in the customized Drone Tools hexarotors, using in both cases the DJI A3 autopilot. The video of the experiments can be seen in the attachment of this paper or in [44]. A sequence of captures taken from the video are depicted in **Fig. 22** and **Fig. 23**. The tests were conducted within a 5×5×3 meters area covered by a safety net, counting with an expert human pilot for correcting eventual height/position deviations of the platform. The autopilot was configured in both cases in Attitude control mode in order to evaluate more clearly the influence of arms motion over the stability of the aerial platform on flight. The height control is based on a barometer. No additional altitude sensor were used

The main purpose of these experiments was to evaluate qualitatively the interactions on flight between the manipulator and the aerial platform when a standard autopilot is employed and there is no feedback from the arms. That is, when the Arms Torque Estimator block in **Fig. 13** is not available. Note that this corresponds to the worst case in terms of control, as the endogenous reactions generated by the arms will be treated by the autopilot as an external perturbation in attitude [22][23]. However, this use case is useful for validating the low weight and inertia features of the arms compared to the multirotor platform, whose weight is four times higher. The visual inspection of the video evidences small deviations in the position of the platform (<0.25 m) when high joint speed motions (250 deg/s) are generated at the shoulder joints, although it is difficult to distinguish the influence of wind perturbations from the displacement associated to the motion of the arms.

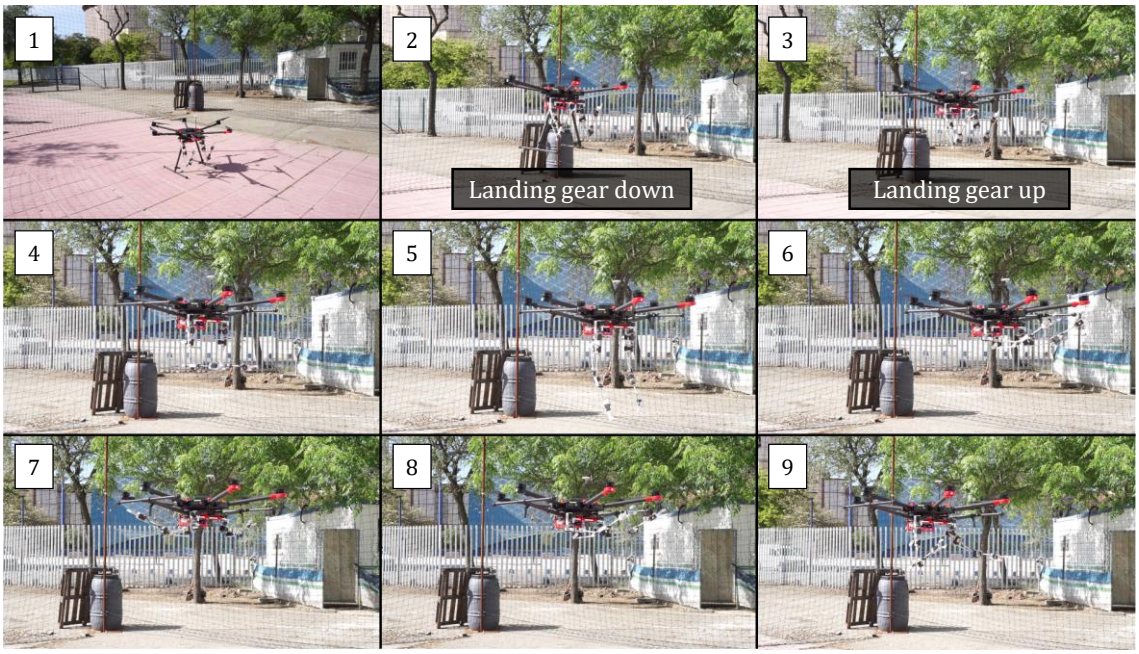

Fig. 22. Sequence of images corresponding to the outdoor flight tests with the arms integrated in the DJI Matrice 600 platform. Platform landed (1), landing gear down – up transition (2 – 3), arms in operation position (4), rotation around the shoulder pitch joint (5 – 6), rotation around the shoulder yaw joint (7 – 8), and left arm fully stretched (9).

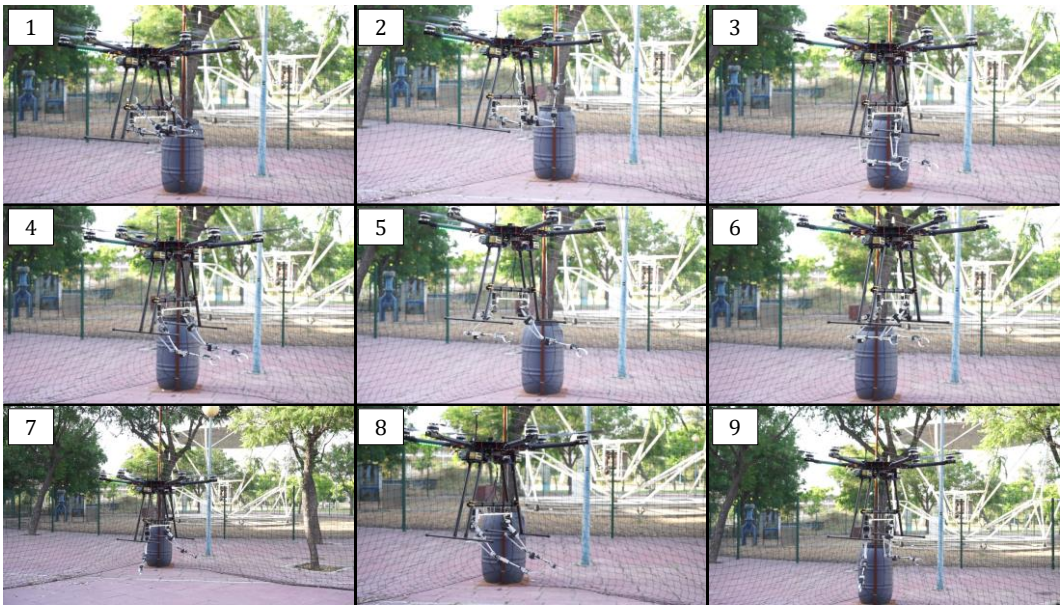

Fig. 23. Sequence of images of the outdoor flight tests with the customized hexarotor manufactured by Drone Tools. Arms in take-off position (1), transition to operation position (2 – 3), execution of different trajectories (4 – 9).

Two relevant conclusions are derived from the analysis of the experiments. First of all, the proposed low weight and inertia dual arm design has been successfully validated on flight. That is, the experiments in the video show that the arms can perform high amplitude (50 cm reach) and high speed motions (up to 300 deg/s) without causing significant displacements over the aerial platform, taking into account that no feedback from the arms was provided to the attitude controller and that no position sensor was employed. The second point to remark is the performance of a standard industrial autopilot properly tuned, as it is capable to keep the platform stable in contactless situations despite the variation of the center of mass and the inertia terms of the reaction wrenches associated to the manipulator.

7. Conclusion and future work

This paper has presented the design of a low weight and inertia, human-size dual arm system designed for aerial manipulation with multi-rotor platform. Each arm, weighting 0.8 kg, provides 3 DOFs for end-effector positioning and 2 DOFs for wrist orientation, with a maximum lift load at wrist point around 0.75 kg. The frame structure of the arms that supports the servo actuators consists of a set of fifty two customized frame parts designed in such a way that they can be easily manufactured in aluminium. The kinematic and dynamic models of the aerial manipulator are derived, proposing a control scheme that copes with the technological limitations of the smart servo actuators. The performance of the arms is demonstrated through the execution of different experiments in a testbench, including trajectory tracking, visual servoing and manual operation. The manipulator has been integrated in two commercial hexarotor platforms and tested in outdoor flights for validating the lightweight design, evaluating qualitatively the influence of arms motion over the UAV when a standard autopilot is employed. The interactions between the arms and the platform were also identified in testbench, hanging the platform from wires emulating hovering conditions, so the reaction torques generated by the arms can be appreciated more clearly.

As future work, authors are working in the modification of the controller implemented by the standard autopilots (DJI, PX4), so a lightweight robot manipulator can be integrated in most commercial multirotor UAVs. We believe that this approach will contribute in the transfer of the aerial manipulation technology and in its application to a wide variety of inspection and maintenance tasks in the industry.

Acknowledgements

This work has been supported by the AEROARMS Project, funded by the European Commission under the H2020 Programme (H2020-2014-644271), the AEROMAIN (DPI2014-59383-C2-1-R) and AEROCROS (DPI2015-71524-R) projects, funded by the Spanish Ministerio de Economia y Competitividad. The research activity of Alejandro Suarez is supported by the Spanish Ministerio de Educación, Cultura y Deporte FPU Program.

References

[1] K. Kondak, F. Huber, M. Schwarzbach, M. Laiacker, D. Sommer, M. Bejar, and A. Ollero. Aerial manipulation robot composed of an autonomous helicopter and a 7 degrees of freedom industrial manipulator, 2014 IEEE International Conference on Robotics and Automation (ICRA), Hong Kong, 2014, pp. 2107-2112.

[2] A. E. Jimenez-Cano, J. Martin, G. Heredia, A. Ollero and R. Cano. Control of an aerial robot with multi-link arm for assembly tasks, 2013 IEEE International Conference on Robotics and Automation, Karlsruhe, 2013, pp. 4916-4921.

[3] M. Orsag, Ch. Korpela, and Paul Oh. Modelling and control of MM-UAV: mobile manipulating unmanned aerial vehicle (2013). Journal of Intelligent and Robotic Systems, Vol. 69, pp. 227-240.

[4] V. Ghadiok, J. Goldin and W. Ren. Autonomous indoor aerial gripping using a quadrotor, 2011 IEEE/RSJ International Conference on Intelligent Robots and Systems, San Francisco, CA, 2011, pp. 4645-4651.

[5] G. Heredia, A.E. Jimenez-Cano, I. Sanchez, D. Llorente, V. Vega, J.A. Acosta and A. Ollero. Control of a multirotor outdoor aerial manipulator, 2014 IEEE/RSJ International Conference on Intelligent Robots and Systems, Chicago, IL, 2014, pp. 3417-3422.

[6] AEROARMS Project Webpage: http://www.aeroarms-project.eu/

[7] ARCAS Project Webpage: http://www.arcas-project.eu/

[8] D. Mellinger, Q. Lindsey, M. Shomin and V. Kumar. Design, modeling, estimation and control for aerial grasping and manipulation, 2011 IEEE/RSJ International Conference on Intelligent Robots and Systems, San Francisco, CA, 2011, pp. 2668-267.

[9] S. Kim, S. Choi and H. J. Kim. Aerial manipulation using a quadrotor with a two DOF robotic arm, 2013 IEEE/RSJ International Conference on Intelligent Robots and Systems, Tokyo, 2013, pp. 4990-4995.

[10] M. Orsag, C. Korpela, S. Bogdan and P. Oh. Valve turning using a dual-arm aerial manipulator, 2014 International Conference on Unmanned Aircraft Systems (ICUAS), Orlando, FL, 2014, pp. 836-841.

[11] ProDrone Webpage: https://www.prodrone.jp/en/archives/1420/

[12] C. D. Bellicoso, L. R. Buonocore, V. Lippiello and B. Siciliano. Design, modeling and control of a 5-DoF light-weight robot arm for aerial manipulation, 2015 23rd Mediterranean Conference on Control and Automation (MED), Torremolinos, 2015, pp. 853-858.

[13] B. Yüksel, S. Mahboubi, C. Secchi, H. H. Bülthoff and A. Franchi. Design, identification and experimental testing of a light-weight flexible-joint arm for aerial physical interaction, 2015 IEEE International Conference on Robotics and Automation (ICRA), Seattle, WA, 2015, pp. 870-876.

[14] A. Suarez, G. Heredia and A. Ollero. Lightweight compliant arm for aerial manipulation, 2015 IEEE/RSJ International Conference on Intelligent Robots and Systems (IROS), Hamburg, 2015, pp. 1627-1632.
[15] G. A. Pratt and M. M. Williamson. Series elastic actuators, Proceedings 1995 IEEE/RSJ International Conference on Intelligent Robots and Systems. Human Robot Interaction and Cooperative Robots, Pittsburgh, PA, 1995, pp. 399-406 vol.1.
[16] A. Suarez, G. Heredia and A. Ollero. Lightweight compliant arm with compliant finger for aerial manipulation and inspection, 2016 IEEE/RSJ International Conference on Intelligent Robots and Systems (IROS), Daejeon, 2016, pp. 4449-4454.
[17] A. Suarez, P. Ramon-Soria, G. Heredia, G., B. C. Arrue, and A. Ollero. Anthropomorphic, compliant and lightweight dual arm system for aerial manipulation, 2017 IEEE/RSJ International Conference on Intelligent Robots and Systems (IROS), Vancouver, 2017.
[18] C. Korpela, M. Orsag, M. Pekala and P. Oh. Dynamic stability of a mobile manipulating unmanned aerial vehicle, 2013 IEEE International Conference on Robotics and Automation, Karlsruhe, 2013, pp. 4922-4927.
[19] F. Caccavale, G. Giglio, G. Muscio, and F. Pierri. Adaptive control for UAVs equipped with a robotic arm. 19th IFAC Proceedings Volumes, *47*(3), 11049-11054, 2014.
[20] G. Arleo, F. Caccavale, G. Muscio and F. Pierri. Control of quadrotor aerial vehicles equipped with a robotic arm, 21st Mediterranean Conference on Control and Automation, Chania, 2013, pp. 1174-1180.
[21] F. Ruggiero, M. A. Trujillo, R. Cano, H. Ascorb, A. Viguria, C. Peréz, and B. Siciliano. A multilayer control for multirotor UAVs equipped with a servo robot arm, 2015 IEEE International Conference on Robotics and Automation (ICRA), Seattle, WA, 2015, pp. 4014-4020.
[22] F. Ruggiero, J. Cacace, H. Sadeghian and V. Lippiello. Impedance control of VToL UAVs with a momentum-based external generalized forces estimator, 2014 IEEE International Conference on Robotics and Automation (ICRA), Hong Kong, 2014, pp. 2093-2099.
[23] T. Tomić and S. Haddadin. A unified framework for external wrench estimation, interaction control and collision reflexes for flying robots, 2014 IEEE/RSJ International Conference on Intelligent Robots and Systems, Chicago, IL, 2014, pp. 4197-4204.
[24] P. E. I. Pounds and A. M. Dollar. Stability of Helicopters in Compliant Contact Under PD-PID Control, in IEEE Transactions on Robotics, vol. 30, no. 6, pp. 1472-1486, Dec. 2014.
[25] G. Giglio and F. Pierri. Selective compliance control for an unmanned aerial vehicle with a robotic arm, 22nd Mediterranean Conference on Control and Automation, Palermo, 2014, pp. 1190-1195.
[26] K. Yoshida, R. Kurazume and Y. Umetani. Dual arm coordination in space free-flying robot, Proceedings. 1991 IEEE International Conference on Robotics and Automation, Sacramento, CA, 1991, pp. 2516-2521 vol.3.
[27] K. Yoshida, R. Kurazume and Y. Umetani. Torque optimization control in space robots with a redundant arm, Intelligent Robots and Systems '91. 'Intelligence for Mechanical Systems, Proceedings IROS '91. IEEE/RSJ International Workshop on, Osaka, 1991, pp. 1647-1652 vol.3.
[28] X. U. Wen-Fu, W. A. N. G. Xue-Qian, X. U. E. Qiang, and B. Liang. Study on trajectory planning of dual-arm space robot keeping the base stabilized. 2013, Acta Automatica Sinica, 39(1), 69-80.
[29] M. Yamano, J. S. Kim, A. Konno, and M. Uchiyama. Cooperative control of a 3d dual-flexible-arm robot. Journal of Intelligent and Robotic Systems, 39(1), 1-15, 2004.
[30] C. Ott, O. Eiberger, W. Friedl, B. Bäuml, U. Hillenbrand, C. Borst, C., ... and R. Konietschke. A Humanoid Two-Arm System for Dexterous Manipulation, 2006 6th IEEE-RAS International Conference on Humanoid Robots, Genova, 2006, pp. 276-283.
[31] F. Caccavale, P. Chiacchio, A. Marino and L. Villani. Six-DOF Impedance Control of Dual-Arm Cooperative Manipulators, in IEEE/ASME Transactions on Mechatronics, vol. 13, no. 5, pp. 576-586, Oct. 2008.
[32] R. C. Luo, B. H. Shih and T. W. Lin. Real time human motion imitation of anthropomorphic dual arm robot based on Cartesian impedance control, 2013 IEEE International Symposium on Robotic and Sensors Environments (ROSE), Washington, DC, 2013, pp. 25-30.
[33] C. Smith, Y. Karayiannidis, L. Nalpantidis, X. Gratal, P. Qi, D. v. Dimarogonas, and D. Kragic. Dual arm manipulation—A survey. Robotics and Autonomous systems, 60(10), 1340-1353, 2012.
[34] M. Grebenstein, A. Albu-Schäffer, T. Bahls, M. Chalon, O. Eiberger, W. Friedl, ... and G. Hirzinger. The DLR hand arm system, 2011 IEEE International Conference on Robotics and Automation, Shanghai, 2011, pp. 3175-3182.
[35] Shadow Dexterous Hand Webpage: https://www.shadowrobot.com/products/dexterous-hand/
[36] E. Papadopoulos. On the dynamics and control of space manipulators. Diss. Massachusetts Institute of Technology, 1990.
[37] E. Papadopoulos and A. Moosavian. Dynamics and control of space free-flyers with multiple manipulators. Advanced robotics 9.6 1994, pp. 603-624.
[38] Bradsky, G.R.: Computer Vision Face Tracking for Use in a Perceptual User Interface (1998)
[39] D. Exner, E. Bruns, D. Kurz, A. Grundhöfer and O. Bimber. Fast and robust CAMShift tracking, 2010 IEEE Computer Society Conference on Computer Vision and Pattern Recognition - Workshops, San Francisco, CA, 2010, pp. 9-16.
[40] Herkulex Servos Webpage: www.dongburobot.com
[41] A. E. Jimenez-Cano, G. Heredia and A. Ollero. Aerial manipulator for structure inspection by contact from the underside, 2015 IEEE/RSJ International Conference on Intelligent Robots and Systems (IROS), Hamburg, 2015, pp. 1879-1884.
[42] R. Munoz-Salinas. ARUCO: a minimal library for Augmented Reality applications based on OpenCv. University of Córdoba (Spain), 2012.
[43] R. Cano, C. Pérez, F. Pruano, A. Ollero, and G. Heredia. Mechanical design of a 6-DOF aerial manipulator for assembling bar structures using UAVs. In 2nd RED-UAS 2013 workshop on research, education and development of unmanned aerial systems, 2013.
[44] Video link to the experiments: https://hdvirtual.us.es/discovirt/index.php/s/7osTL1BO7XkkJKD